Department of Advanced Materials Science,
Graduate School of Frontier Sciences,
The University of Tokyo
2022
Master's Thesis

Efficient Orbital Torque in Polycrystalline Ferromagnetic-metal/Ru/Al_2O_3 Stacks

多結晶強磁性金属/Ru/Al_2O_3 積層構造における高効率軌道トルク

Submitted July 19, 2022

Advisor: Professor Yoshichika Otani

Liyang Liao

Abstract

Electrical control of nanomagnet is the key to developing spintronic memory and logic devices. Current-induced torque effects, especially the spin-orbit torque, have been vigorously investigated in the last decade to achieve energy-efficient manipulation of nanomagnets. Recently emergent current-induced orbital torque is considered more effective for magnetization switching than the well-established spin-orbit torque. However, understanding the orbital transport in polycrystalline heterostructures remains elusive.

This thesis focuses on the current-induced torque effect in CoFeB/Ru/Al_2O_3 polycrystalline stacks to clarify the underlying physics of orbital transport. The unfilled *d*-shell and small spin-orbit coupling in Ru enable the orbital generation and transport. The orbital current from the Ru/Al_2O_3 interface can go through a thick Ru layer with the peak value at 7 nm-thick Ru and then exert the strongest torque for CoFeB. The magnitude of the observed torque effect can be larger than that in the commonly used heavy metal Pt in conventional spin-orbit torque devices (torque efficiency ~0.1). The observed torque efficiency increases with increasing CoFeB layer thickness, leveling off at ~0.3 for 12 nm-thick CoFeB. By varying the Ru thickness, the origin of the orbital current is identified to be the Ru/Al_2O_3 interface.

The orbital generation and propagation are modeled by tight-binding calculation and quantum evolution simulation, supporting the observation of the torque effect. Theoretical analysis shows that the orbital transport in polycrystalline materials exhibits a random precession behavior, leading to a more efficient orbital transport than in single crystals. The findings demonstrate that transition metal with unfilled d-shell and small SOC provides an ideal platform for orbital torque induced by the orbital Rashba effect, which may contribute to the research on orbital transport and the development of orbital torque devices.

Table of contents

1. Introduction

1.1 Spintronics and orbital torque

The development of micro-nano electronics and information communication technology has brought the information and Internet era to human beings. For this advancement, magnetic materials and spintronics devices have already played some role. Hard disk read heads based on Giant Magnetoresistance (GMR) and Tunneling Magnetoresistance (TMR) effects are precursors of spintronic applications. They have made a critical contribution to the improvement of storage density. In recent years, Magnetic Random Access Memories (MRAMs), operated by Spin Transfer Torque (STT) and Spin-Orbit Torque (SOT), have also received intensive attention because of their potential application for computer memory and significant technical reserves of hard disks. Since magnetism is non-volatile, spintronic devices also have considerable potential in the Internet of Things, artificial intelligence, probabilistic computing, communication, and filtering technologies.

The efficient electrical control of magnetic states in the nanoscale magnet is strongly requested to develop spintronic memory and logic devices. During the last decade, the SOT has been actively studied to efficiently manipulate nanomagnets. As shown in Fig. 1.1, the device operated by the SOT consists of a nonmagnetic metal (NM)-ferromagnet (FM) bilayer, where the nonmagnetic metal has sizable spin-orbit coupling (SOC). By injecting the charge current in the bilayer, the spin current is generated by the spin Hall effect in the heavy metal. The spin current is then injected into the adjacent FM, and the angular momentum transfer between the spins and the magnetization results in a torque on the magnetization [1,2]. Such torque is called SOT. The SOT can switch the magnetization, and serve as the write-in technique for MRAMs.

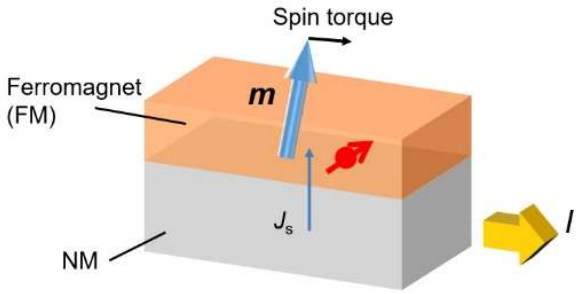

Fig. 1.1 Illustration of the SOT induced by the spin Hall effect.

As an alternative mechanism for spin manipulation, the utilization of the orbital angular momentum has been considered recently [3–8]. Unlike the spin current generation for the SOT [Fig. 1.2(a)], the orbital current generation for the OT does not require the sizeable strength of the SOC. Orbital current can be generated directly from orbital texture, e.g., the band structure of *s*-*d* hybridization. When the orbital source material is attached to a magnet with a sizeable SOC, the current in the orbital source material can inject an orbital current into the magnet, and the orbital current can exert a torque on the magnetization via SOC, as shown in Fig. 1.2(b).

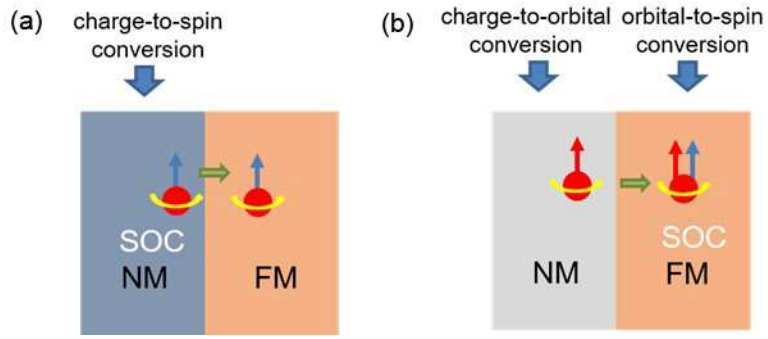

Fig. 1.2 Illustration of the SOT (a) and OT (b).

Owing to the angular momentum conservation law, one needs to inject sufficient angular momentum into the magnet to manipulate the magnetization orientation. As the spin current carries at most $\hbar/2$ angular momentum with each electronic state, the orbital current can carry more angular momentum with each electronic state. In a naïve sense, for *p*, *d*, *f*, … electrons, the maximum angular momenta they can transfer are $\hbar$, $2\hbar$, $3\hbar$, …, respectively. This consideration makes it appealing to utilize the orbital current instead of the spin current to manipulate nanomagnets.

1.2 Motivation

According to theoretical studies, the orbital current would be generated much more efficiently than its spin counterpart in most metals [9,10]. In the equilibrium state, the orbital quenching effect leads to zero orbital polarization. However, when an electric field is applied, orbital current or orbital polarization can be induced due to the orbital hybridization, such as the *s*-*p* or *s*-*d* hybridization [9]. The charge current-induced orbital current has the same geometry as the spin Hall effect [Fig. 1.3(a)]. As shown in Fig. 1.3(b), flowing of the orbital current is described by a relation $j_{\text{orbital}} = k \times p$, where k is the wavevector and p is the orbital polarization. This is called the orbital Hall effect (OHE) [9,10]. At an inversion-symmetry-breaking interface with orbital hybridization, a k-dependent orbital polarization can be formed in the interfacial states, known as the orbital Rashba effect (ORE) [11,12]. Similar to the spin polarization in the spin Rashba effect [Fig. 1.3(c)], the orbital polarization p is described by $p = k \times z$, where z is the normal direction of the interface in the ORE [Fig. 1.3(d)]. Since a charge current creates asymmetric occupation of the interfacial states, an orbital polarization can be generated by an in-plane charge current, called the orbital Edelstein effect [5,6]. The materials selected for the orbital source are extensive due to the unnecessity of the SOC [13,14], in contrast to the limited material selection for the spin current generation (a few kinds of heavy elements such as Pt, Ta, W, and Bi). The orbital current also has the characteristic of long propagation length in FMs because, in ferromagnets, the dephasing of the orbital current is controlled by the weak SOC instead of the strong *s*-*d* interaction that governs the spin current dephasing [15]. Therefore, the orbital current has the potential to manipulate thick FMs.

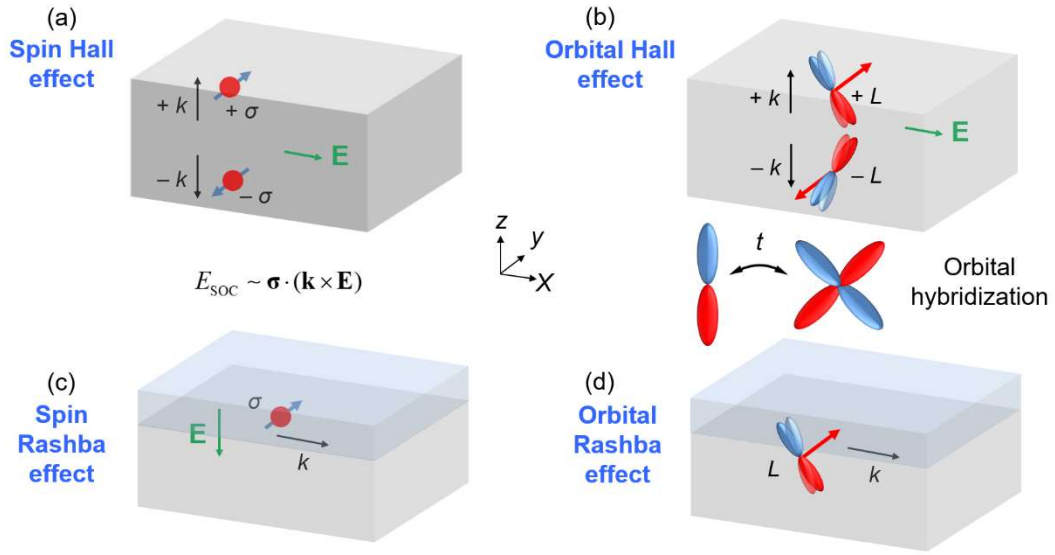

Fig. 1.3 Illustration of the spin Hall effect (a), orbital Hall effect (b), spin Rashba effect (c), and orbital Rashba effect (d).

Recently, many experimental reports claimed that the observed torque in FMs originated from the action of the orbital angular momentum. In a Pt/Co/SiO_2 stack, a large current-induced torque is interpreted by orbital hybridization at the Pt/Co and Co/SiO_2 interface [5]. In ferromagnet (FM)/Cu/CuO_x [6] and FM/Cu/Al_2O_3 [4] stacks, large torque that strongly depends on the kind of FM layer was observed and explained by the orbital Rashba effect. In TmIG/Pt/CuO_x trilayer, the current-induced torque efficiency can be firmly tuned by thin Pt layer insertion, which is also understood by the orbital picture [8]. Long-range orbital transport in FMs was also reported by the Orbital Rashba-Edelstein magnetoresistance [16]. The competition between SOT and OT was revealed in various magnetic bilayers [3,7].

Industrial on-silicon production requires the development of OT devices based on polycrystalline stacks. In previous reports, OT was experimentally observed in polycrystalline stacks prepared by room temperature evaporation or sputtering, mainly based on the interfacial orbital Rashba effect (ORE) [4,8]. The OT can be controlled and distinguished from other torque mechanisms by designing different layer structures. In these reports, an interface containing Cu or Pt is utilized as a source of the orbital angular momentum. However, the filled *d*-shell of Cu and the large SOC of Pt would hinder the orbital transport, and complicate the analysis of OT in polycrystalline stacks, respectively. It is also reported that the orbital transport in Cu is assisted by oxidation [6,17], which surely would provide complexity to the

structure. Meanwhile, theoretical works have focused on the orbital generation and transport in single crystalline structures to avoid the complexity of polycrystalline heterostructures. It is highly warranted to bridge the gap between the experiment and theory by studying the orbital transport in polycrystalline stacks.

This thesis experimentally studies the current-induced orbital torque in polycrystalline FM/Ru/Al_2O_3 stacks (Fig. 1.4). Ru is chosen because of its electronic configuration ($4d^7 5s^1$) and the low efficiency of the spin current generation from the charge current. In the FM/Ru/Al_2O_3 stacks, the orbital current generation is expected by the orbital hybridization at the Ru/Al_2O_3 interface. The orbital current propagation in the Ru layer would be efficient considering the presence of *d* electrons at the Fermi level. The weak SOC in Ru helps to reduce the SOC-related orbital relaxation and the conventional spin Hall torque [18] that may interfere with the identification of the OT. We also construct a theoretical model for the orbital generation and transport in polycrystalline stacks.

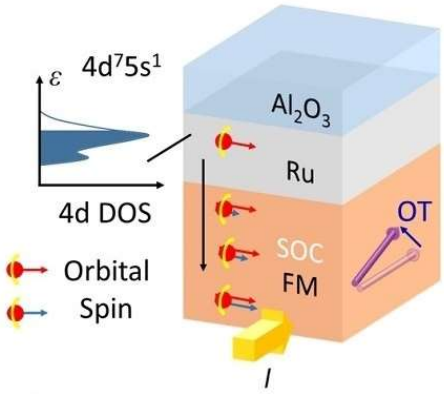

Fig. 1.4 Schematic of the orbital torque in FM/Ru/Al_2O_3.

1.3 Outline

The following part of this thesis is structured as follows:

Charter 2 describes the experimental methods used in this study, including the thin film deposition, sample characterization, device fabrication, and measurements. The basic properties of the samples were characterized by using a transmission electron microscope (TEM) and vibrating sample magnetometer (VSM); the current-induced torque effect is studied by spin-torque ferromagnetic resonance (ST-FMR), spin pumping, and second-harmonic transport measurements.

Charter 3 systematically discusses the results in samples with different structures and layers. It includes experimental results from studies on various FM components, FM layer thickness, and the Ru thickness. A significant current-induced torque effect is observed in FM/Ru/Al_2O_3 stacks and attributed to the ORE and orbital Edelstein effect at the Ru/Al_2O_3 interface.

Charter 4 develops theoretical models for the orbital generation and orbital propagation. Tight-binding model is employed for the ORE and orbital Edelsgtein effect at the Ru/Al_2O_3 interface. An orbital hopping model with a quantum evolution equation is developed for the orbital transport.

Charter 5 is the conclusion, followed by the publication and acknowledgment parts.

2. Experimental methods

2.1 Thin film deposition

In this work, thin-film samples were prepared by magnetron sputtering. Magnetron sputtering works in an Ar atmosphere, using coexisting electric and magnetic fields to control the motion of the Ar^+ ions and the sputtered particles, as shown in Fig. 2.1.

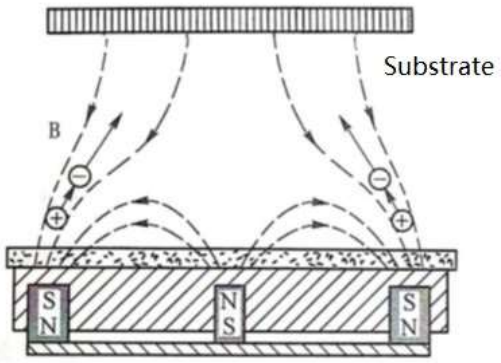

Fig. 2.1 Schematic of the sputtering deposition.

We prepared thin films with a multi-target sputter chamber made by AJA Inc.. FM(t_F)/Ru(t_{Ru})/Al_2O_3(2), FM(t_F)/Ru(t_{Ru}) and FM(t_F)/Pt(1)/Ru(t_{Ru})/Al_2O_3(2) multilayers (thickness in nm) were grown on a thermally oxidized Si/SiO_2 substrate at room temperature, where FM = $Co_{40}Fe_{40}B_{20}$ (CoFeB) or $Ni_{81}Fe_{19}$ (NiFe), t_F varies

from 5 to 18 nm, and t_{Ru} varies from 1.5 nm to 9 nm. All metallic layers were deposited by DC sputtering at 50 W and the Al_2O_3 layer was deposited by RF sputtering at 150 W, with a working pressure of 0.4 Pa and a base pressure of $< 1\times10^{-5}$ Pa.

2.2 Sample characterization

In this work, we investigate ultra-thin polycrystalline films, whose structure is hard to be characterized by the X-ray diffraction observation. Instead, we adopt the transmission electron microscope (TEM) observation to check the sample structure. A piece of cross-sectional slide of SiO_2/CoFeB(7)/Ru(6)/Al_2O_3(2) sample was prepared by focus ion beam fabrication. As shown in TEM image (Fig. 2.2), both the Ru and the Al_2O_3 layers display the polycrystalline nature. Here crystalline structures are clearly shown, but their crystal orientations change dependent on position. Also, we cannot find clear grains with ~ 10–100 atoms in one dimension. We hence conclude that the grain size of Ru is tiny. The CoFeB layer is closer to an amorphous state, possibly due to alloy instead of elemental metal.

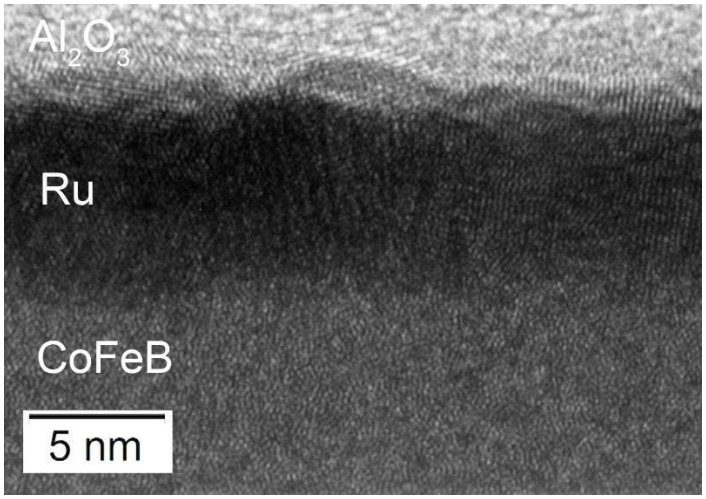

Fig. 2.2 Cross-sectional transmission electron microscope image of CoFeB(7)/Ru(6)/Al_2O_3(2).

The magnetic properties of the samples were characterized by vibrating sample magnetometer (VSM). Fig. 2.3 shows the M-H curves of CoFeB(7)/Ru(6)/Al_2O_3(2) sample (a) and NiFe(7)/Ru(6)/Al_2O_3(2) sample (b). The CoFeB has a larger saturation magnetization (15 kOe) than that for the NiFe (7 kOe).

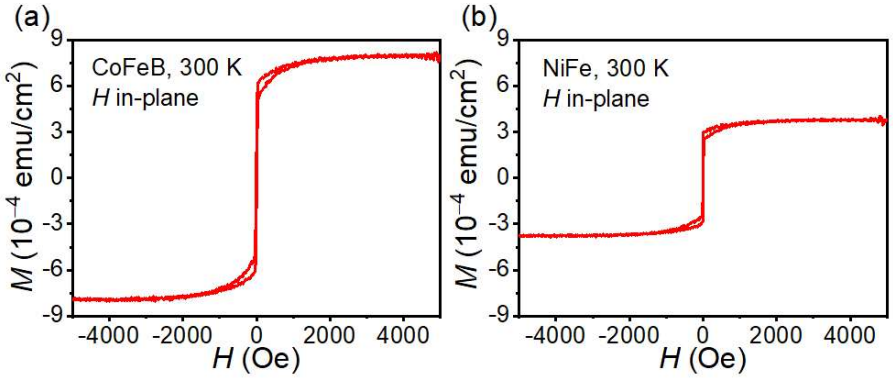

Fig. 2.3 Vibrating Sample Magnetometer (VSM) data of (a) CoFeB(7)/Ru(6)/ Al_2O_3(2) and (b) NiFe(7)/Ru(6)/Al_2O_3(2).

2.3 Device fabrication

After the thin film deposition, we fabricate ST-FMR devices to characterize the current-induced torque efficiency in these stacks. In ST-FMR measurements, we inject a ratio-frequency current into the device channels made by the FM/Ru/Al_2O_3 films. In the first step, channels (length, 60 μm; width 20 μm) were patterned using photolithography. We used positive photoresist AZ5214e to fabricate the devices. After spin coating the photoresist on the film, the samples are baked at 95°C for 90 s. Then, the samples are covered by a mask with the device patterns and exposed to ultraviolet light for 23 s. The positive photoresist in the areas covered by the mask would be protected, whereas the exposure would modify the photoresist in other areas. Next, the samples were put into the NMD-3 developer for 20 s, which can dissolve the modified photoresist and leave an unmodified photoresist. Hence, the patterns of the device channels were formed on the thin film with the photoresist.

In the second step, Ar ion-milling was used to etch the films. During the milling process, the device channel areas protected by the photoresist would be kept, and the films in other areas would be etched. Ar ion-milling was performed in a vacuum chamber similar to the sputtering. After the milling, the photoresist was dissolved by acetone.

In the final step, photolithography and lift-off process prepared coplanar waveguides made of Ti (10nm)/Au(140nm). In this photolithography step, photoresist windows were defined by the ultraviolet light exposure in the waveguide areas. After the development, the photoresist in the waveguide areas were dissolved and the photoresist outside the window remains. Then Ti (10nm)/Au(140nm) films was deposited by e-beam evaporation. After the deposition, the remaining photoresist was dissolved by acetone, and the covering Ti/Au film was also removed simultaneously. With similar steps, spin pumping devices and Hall bar devices were also fabricated for supporting measurements.

2.4 Ratio frequency measurements

The current-induced torque effect is studied by spin-torque ferromagnetic resonance (ST-FMR) [Fig. 2.4]. In ST-FMR measurement, a modulated ratio frequency (rf) current from 6 GHz to 11GHz was applied along the device channel, with amplitude 19 dBm (for CoFeB samples) or 16 dBm (for NiFe samples). The mixing voltage (A – B) was measured by a SR830 lock-in amplifier, with a reference signal (ref) with the modulation frequency. The angle φ between the external magnetic field $\boldsymbol{H}$ and the longitudinal direction of the channel is 45°.

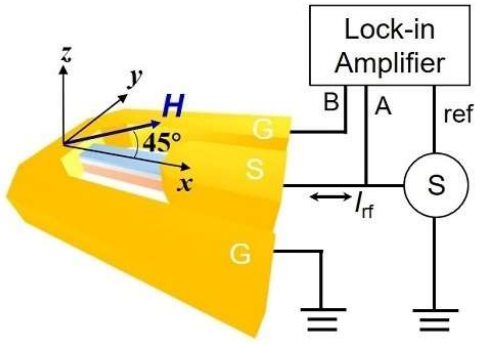

Fig. 2.4 Experimental setup of the ST-FMR measurement.

ST-FMR measurement is based on the ac-current induced nonequilibrium oscillation of the magnetization. If a current I in the magnetic multilayer can induced a torque $\boldsymbol{\tau}$ on the magnetization, an ac current $I = I_0 \exp(i\omega t)$ will induce an ac torque $\boldsymbol{\tau} \exp(i\omega t)$. The magnetization would be driven into procession by this oscillating torque, and the procession amplitude will be the largest when the current frequency ω meet the resonance condition. Due to the anisotropy magnetoresistance (AMR) effect, the procession of the magnetization will change the longitudinal resistance of the ST-FMR device with the same frequency ω. Since both resistance and current change with frequency ω, a mixing dc voltage would be produced, and can be measured by a lock-in amplifier, as shown in Fig. 2.4. The rf current was modulated, and a reference signal with the modulation frequency was sent to the lock-in amplifier as the reference-in signal.

The fitting function of the ST-FMR signal is

$$V_{\text{mix}} = S\frac{\Delta^2}{(H-H_0)^2+\Delta^2} + A\frac{\Delta(H-H_0)}{(H-H_0)^2+\Delta^2}, \quad (2\text{-}1)$$

where H is the applied magnetic field, H_0 is the resonance field, and Δ is the linewidth. The symmetric component S comes from the antidumping-like torque, and the antisymmetric component A comes from the field-like torque and the Oersted field.

The resonant field follows Kittel formula

$$f = \frac{\gamma}{2\pi}\sqrt{H_0(4\pi M_{\text{eff}} + H_0)}\text{ , (2-2)}$$

2here γ is the gyromagnetic ratio and M_{eff} is the demagnetization field. The antisymmetric and symmetric component A and S are related to the out-of-plane torque $\tau_{\perp}$ and the in-plane torque $\tau_{//}$, respectively.

$$A = -\frac{\gamma I_{\text{rf}} \cos\theta}{4\Delta}\frac{dR}{d\theta}\sqrt{1+\frac{4\pi M_{\text{eff}}}{H}}\tau_{\perp} \text{(2-3)}$$

$$S = -\frac{\gamma I_{\text{rf}} \cos\theta}{4\Delta}\frac{dR}{d\theta}\tau_{//} \text{(2-4)}$$

Combining Eq. (2-3), Eq. (2-4) and the geometric relationship between torque and spin polarization, ST-FMR allows one to distinguish field-like and damping-like torque from both in-plane and out-of-plane spin polarization through angular dependence measurement.

In the simplest case, the in-plane torque $\tau_{//}$ is only originated from the damping-like torque of an in-plane spin polarization produced by spin Hall effect (SHE) and the out-of-plane torque $\tau_{\perp}$ is produced by Oersted field. Since the Oersted field can be calculated from Ampe`re's law, it can serve as a calibration of the current density in the nonmagnetic spin source layer and the ratio of spin current density and charge current density can be calculated in a simple way from the ratio of the symmetric and antisymmetric components

$$\frac{j_{\text{L}}}{j_{\text{C}}} \approx \xi_{\text{FMR}} = \frac{S}{A}\frac{4\pi M_{\text{s}} e t_{\text{F}} t_{\text{Ru}}}{\hbar}\left[1+\frac{4\pi M_{\text{eff}}}{H_0}\right]^{1/2}\text{ , (2-5)}$$

where j_{L} is the angular momentum current density absorbed by the FM layer, j_{C} is the charge current density in the Ru layer, M_{s} is the saturated magnetization, e is the elementary charge, $\hbar$ is the reduced Planck constant, t_{F} is the thickness of the FM layer, and t_{Ru} is the thickness of the Ru layer.

It should be noted that the field-like torque from in-plane spin accumulation can also produce anti-symmetric voltage signal. The coexistence of Oersted and field-like torque may lead to an unphysical ferromagnet thickness dependence of the charge-spin conversion efficiency calculated by Eq. (2-5). Another artifact is that rf Oersted

field can drive spin pumping and give a symmetric dc voltage signal through inverse spin Hall effect (ISHE). This phenomenon can bring considerable error to the measured efficiency when the AMR is small [19].

Typical ST-FMR spectra are shown in Fig. 2.5(a) and (b). When sweeping the magnetic field, the mixing voltage shows a Lorentz peak at the resonance condition. When frequency increases, the resonance field increases. The ST-FMR signal is antisymmetric for negative field [Fig. 2.5(a)] and positive field [Fig. 2.5(b)], consistence with the experimental setup and sample structure without symmetric breaking.

The Kittel fitting of the resonance field-frequency curve using Eq. (2-2) [Fig. 2.5(c)] yields a $4\pi M_{eff} = 15.7$ kOe, close to the saturated magnetization measured by VSM [Fig. 2.3(a)], showing that the in-plane anisotropy of the film is mainly contributed by the demagnetization field. The linewidth of the Lorentz lineshape enhances linearly with increasing frequency [Fig. 2(c)]. The small linewidth value and slope suggest that the film has a small damping constant. Fig. 2.4(e) shows the calculated ξ_{FMR} using Eq. (2-5). It can be seen that $\xi_{FMR} \approx 0.3$ at all frequency, showing good consistency.

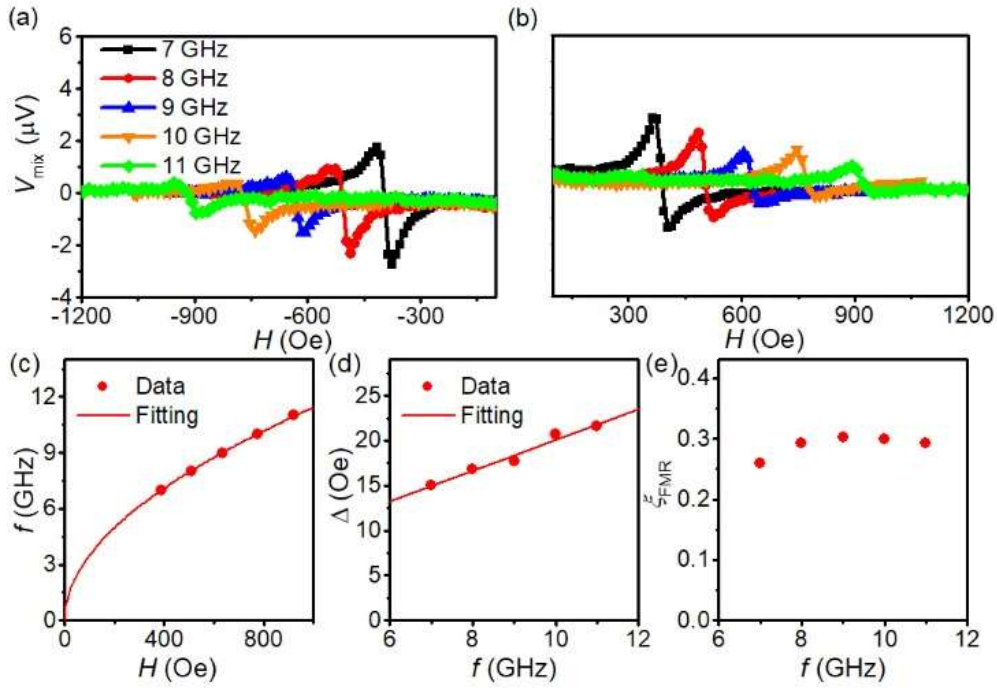

Fig. 2.5. (a) ST-FMR spectra of CoFeB(12.2)/Ru(7)/Al_2O_3(2) at 7-11 GHz with negative field. (b) ST-FMR spectra of CoFeB(12.2)/Ru(7)/Al_2O_3(2) at 7-11 GHz with positive field. (c) Kittel fitting of the resonance condition. (d) Linewidth of the ST-FMR data at 7-11 GHz in the CoFeB(12.2)/Ru(7)/Al_2O_3(2) device. (e) Calculated ζ_{FMR} from the ST-FMR data with different rf frequency.

We also performed spin pumping measurements to exclude their contribution to the ST-FMR. In spin pumping measurement, ferromagnetic multilayer strips are placed between the signal line and the ground line of a coplanar waveguide. When rf current is applied in the coplanar waveguide, rf magnetic field acts on the ferromagnetic multilayer strips. A magnetic field is applied perpendicular to the strips at the same time. When the frequency of the rf current and the external magnetic field meet the resonance condition given by Eq. (2-2), the magnetization will start the ferromagnetic resonance. The ferromagnetic resonance leads to nonequilibrium spin accumulation at the FM/NM interface, resulting in spin injection from the FM to the NM, called spin pumping. A voltage signal is generated when the NM or the NM/oxide interface in the FM/NM/oxide trilayer can convert spin current into charge current. The spin pumping induced voltage signal changes sign when the magnetic field is reversed because of the reversed spin accumulation direction.

As shown in Fig. 2.6, in a controlled sample NiFe/Pt, spin pumping peaks appear at the ferromagnetic resonance fields. In NiFe/Pt/Ru/Al_2O_3, the spin pumping peaks also exist but are smaller than the NiFe/Pt. Due to the large AMR of NiFe, the spin pumping contribution in the ST-FMR measurement in NiFe/Pt is small [19]. The NiFe/Pt/Ru/Al_2O_3 should have similar situation. In the main sample for this study, the CoFeB/Ru/Al_2O_3, we cannot find clear spin pumping peaks. It ensures that the ST-FMR measurement of CoFeB/Ru/Al_2O_3 is hardly modulated by the spin-pumping.

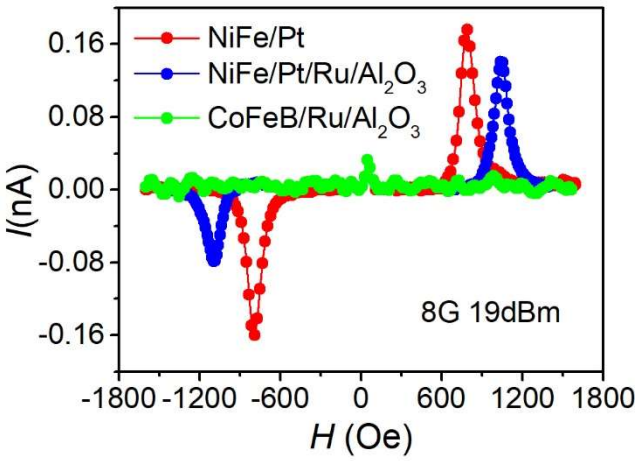

Fig. 2.6. Spin pumping results of NiFe(7)/Pt(4), NiFe(7)/Pt(1)/Ru(6)/Al_2O_3(2) and CoFeB(7)/Ru(6)/Al_2O_3(2). The absence of the spin pumping signal ensures that the ST-FMR signal would not be interrupted by the spin pumping signal.

2.5 Transport measurements

We performed a second-harmonic transport measurement on Hall bar devices on the FM/Ru/Al_2O_3 stacks to obtain additional independent evidence for the current-induced torque effect. The device structure and the measurement setup are given in Fig. 2.7(a). The dimension of a Hall bar device on the CoFeB(12.2)/Ru(7)/Al_2O_3(2) stack is 10 μm× 30 μm. And longitudinal resistance of this device is 25.5 Ω. The current is along the *x* direction, and the *z* direction is the normal direction of the sample surface. The rotation angles in the *yz* and *xz* planes are defined as β and γ, respectively. Figure 2.7(b) shows the β and γ scan of the first harmonic magnetoresistance. The β scan yields a 'w' shape curve, i.e., a signal with a period of 180° and smaller resistance under an in-plane magnetic field. This is the typical behavior for spin-Hall-magnetoresistance or Edelstein magnetoresistance, consistent with the literature [20]. The γ scan corresponds to the AMR signal. The observed signal also has a period of 180°, and the maximum occurs under in-plane magnetic

field, consistent with the AMR effect [20]. The difference at $\beta = 90°$ and $\gamma = 90°$ gives the in-plane magnetoresistance = 0.06%.

The unidirectional spin-Hall magnetoresistance (USMR) alternatively supports the current-induced torque. The USMR originates from the asymmetric scattering between the current-induced nonequilibrium spin accumulation σ and the magnetization M, similar to the giant magnetoresistance: the *s*-*d* scattering rate is different for σ parallel to M and σ antiparallel to M. Since the USMR is proportional to the applied current I, the resulting voltage signal is hence proportional to I^2, i.e., a second-harmonic signal.

Fig. 2.7(c) displays the β angle dependence of the second-harmonic R_{xx} and γ angle dependence of the second-harmonic R_{xy} with current = 10 mA, corresponding to current density 1.7×10^6 A/cm^2, under the applying external field = 20 kOe. Different from the first harmonic signal, the second harmonic signal shows a period of 360°, and have maximum and minimum at 90° and 270°, respectively. The observed second harmonic R_{xx} is consistent with the previously reports on the USMR [21], which has maximum and minimum at 90° and 270° respectively because M is parallel or antiparallel to σ respectively. Beside the USMR, the thermal effect can also contribute to the signal with the same symmetry. However, in the transverse resistance R_{xy} includes the thermal contribution but not for the USMR contribution. Thus the thermal contribution in the R_{xx} signal can be subtracted by $-l/w\ R_{xy}$, where l and w are the length and width of the device, respectively. It can be seen that R_{xx} is much larger than $-l/w\ R_{xy}$, demonstrating the USMR contribution in the R_{xx} measurement. When fixed the angle at 90° and swapped the magnetic field, the signal difference at positive and negative field [Fig. 2.7(d)] is consistent with the signal difference at 90° and 270°. The current dependence of the second-harmonic signals are summaried in Fig. 2.7(e). The slope of the R_{xy} signal under γ rotation represents the thermal contribution in the USMR measurement, and the difference between the R_{xx} slope and the R_{xy} slope represents the USMR effect. The sizable USMR signal further confirms the

existance of the current-induced torque in the CoFeB/Ru/Al_2O_3 stack supporting the ST-FMR measurent results in section 2.4.

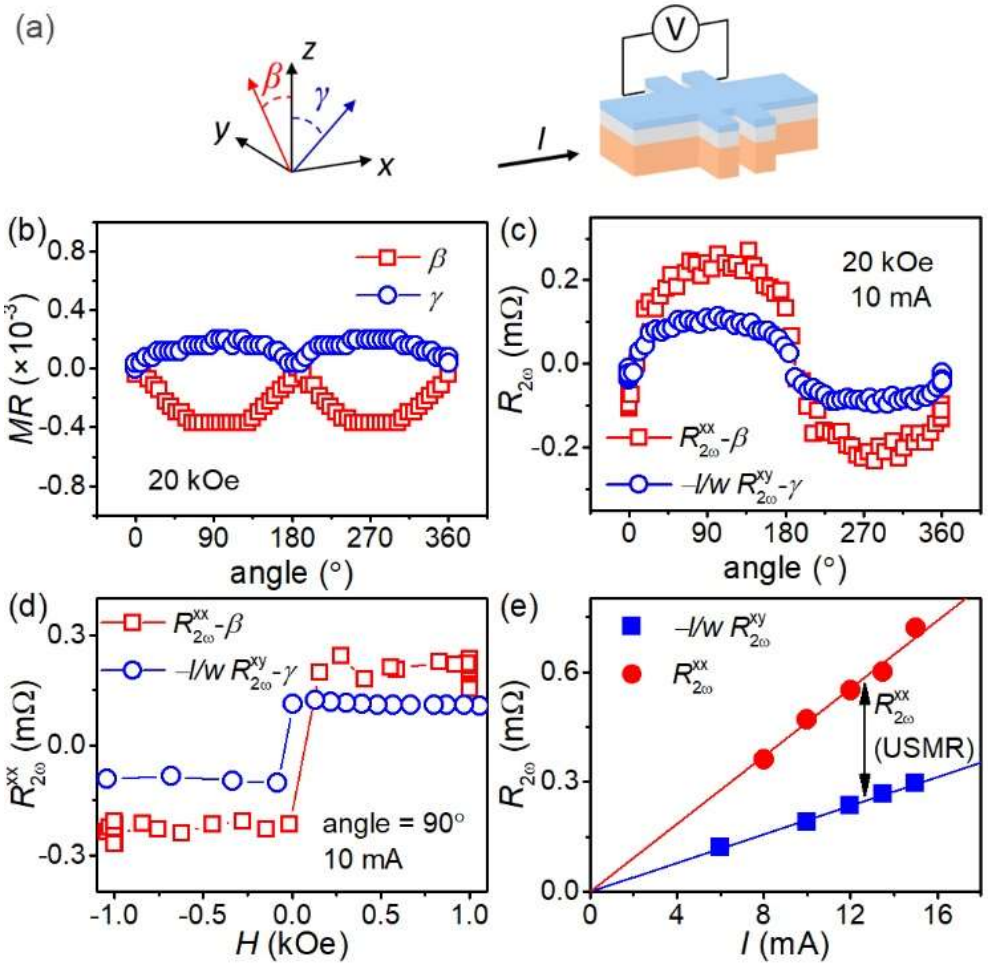

Fig. 2.7. Unidirectional spin-Hall magnetoresistance (USMR) measurements. (a) Geometric of the transport measurement. (b) The magnetoresistance measured with β and γ rotation. (c) β angle dependence of the second-harmonic R_{xx} and γ angle dependence of the second-harmonic R_{xy}. (d) Magnetic field dependence of the second-harmonic R_{xx} with $\beta = 90°$ and the second-harmonic R_{xy} with with $\gamma = 90°$. (e) Current dependence of the second-harmonic signals.

3. Orbital torque in Ru-based multilayer

3.1 Torque in Ru-based multilayers

We now systematically discuss the experimental results and discuss the the revealing OT behaviors in Ru-based multilayers. In Fig. 3.1(a), we show the V_{mix} signal obtained from the ST-FMR measurement of CoFeB(7)/Ru(6)/Al_2O_3(2) stack (units in nanometers) trilayer. The current-induced torque drives magnetization precession at the resonance condition, giving rise to a resonance peak. The ST-FMR spectrum is fitted by the asymmetric (A) and symmetric (S) components of Lorentzian. As shown in Fig. 3.1(a), a sizable negative S component is observed for the CoFeB(7)/Ru(6)/Al_2O_3(2) stack, demonstrating the existence of the current-induced damping-like torque. Note that the small amplitude of the resonance signal is due to the small in-plane magnetoresistance (~0.06%) of CoFeB, and the possible spin pumping contribution to S is excluded. We also note that the thick CoFeB layer and the large demagnetization field hinder obtaining a sizeable signal from the USMR technique. Hence, the torque efficiency is mainly evaluated by analyzing ST-FMR spectra.

Utilizing the ST-FMR spectrum, we evaluate the current-induced torque efficiency ξ_{FMR} with Eq. (2-5). We found that the sign of observed A is unchanged for all devices, keeping consistent with the Oersted field torque. It supports the restricted or negligible contribution of the field-like torque for the A component in the thick FM thickness regime. For the CoFeB(7)/Ru(6)/Al_2O_3(2) stack, ξ_{FMR} is evaluated to –0.15, which is even larger than the spin torque efficiency of the widely used heavy metal Pt (~0.1). In contrast, the S component becomes much smaller in CoFeB(7)/Ru(6) [Fig. 3.1(b)], corresponding to ξ_{FMR} = –0.04, less than one-third of that in the sample with the Al_2O_3 capping. These contrast values of ξ_{FMR} indicate that the generation of the orbital current dominantly comes from the Ru/Al_2O_3 interface rather than the CoFeB/Ru interface or the bulk Ru layer.

Interestingly, less than five times smaller $|\xi_{FMR}|$=0.03 is observed for the $Ni_{80}Fe_{20}$/Ru(6)/Al_2O_3(2), where only the ferromagnetic metal (FM) layer is replaced from CoFeB to $Ni_{80}Fe_{20}$. [Fig. 3.1(c)]. Such a large difference is hard to be explained by the different interfacial transparencies depending on the FMs; instead, it indicates that the generation mechanism of the large torque is deeply linked to the FM layer. On the contrary, we obtain a large and positive S component corresponding to ξ_{FMR} = 0.08 after inserting a thin Pt layer (1 nm) between NiFe and Ru layers [Fig. 3.1(d)]. The distinct torque efficiency dependent on the FM could be originated from the different orbital-to-spin conversion efficiency $\eta_{L\text{-}S}$, which is also related to the spin

Hall effect (SHE) and the anomalous Hall effect (AHE). In literature, we find that negative SHE of CoFeB. Also, numbers of effect originated by SOC, e.g. AHE and spin-rotation coupling, in NiFe with composition rate around Ni:Fe = 80:20 are commonly very small, possibly deeply connected to opposite sign of AHE between polycrystalline Ni and Fe. Therefore, an extra layer is required to obtain large torque when FM=NiFe, and it is realized after inserting the Pt layer with large and positive $\eta_{L\text{-}S}$. In an experimental study, the opposite sign of OT is observed between Fe/Cu/CuOx and NiFe/Cu/CuOx. However, the first-principle calculation gives a positive sign $\eta_{L\text{-}S}$ for single crystalline Fe, Co, and Ni, which can also explain some OT experiments. Likely, these conflicting assertions reflect that the orbital-to-spin conversion could be critically determined by material conditions, e.g., single- or poly-crystalline state of FMs, or elementary and alloy FMs.

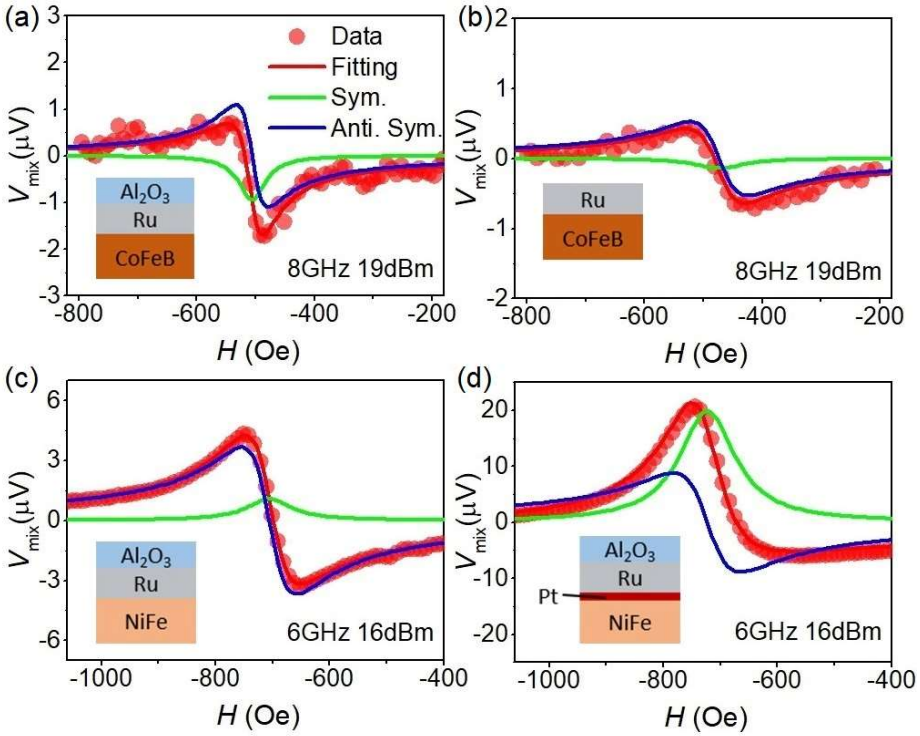

Fig. 3.1. (c)–(f) are the ST-FMR spectra and fitting for (c) CoFeB(7)/Ru(6)/Al_2O_3(2) and (d) CoFeB(7)/Ru(6) devices at 8 GHz, and (e) NiFe(7)/Ru(6)/Al_2O_3(2) and (f) NiFe(7)/Pt(1)/Ru(6)/Al_2O_3(2) devices at 6 GHz. The red circles are experimental data, and the red lines are fitting curves. The symmetric and antisymmetric components are plotted in the right panel with green and blue lines, respectively. Schematics of the sample layout are shown in the inset.

3.2 Ferromagnet thickness dependence

The thickness of FM could be a factor for ξ_{FMR} considering that the orbital-to-spin conversion occurs in the FM layer. The ST-FMR spectra of CoFeB(t)/Ru(6)/Al_2O_3(2) stack with various CoFeB film thicknesses (t_F = 4.8–17.8 nm) is presented in Fig. 3.2(a). Concomitant ξ_{FMR} and $4\pi M_{eff}$ are summarized in Fig. 3.2(b). The comparable M_{eff} reflects similar magnetic properties for the CoFeB layer in all of the samples. Note that $|\xi_{FMR}|$ increases with the increase of the CoFeB layer thickness and finally reaches a saturation value ~0.3 at t_F = 12.6 nm. Meawhile, the contribution of the field-like torque could lead to the overestimation of ξ_{FMR}. We never find a sign change of the A component in the CoFeB(t_F)/Ru(6)/Al_2O_3(2) stack keeping with consistent to sign of the Oersted field torque. [Fig. 3.2(a)]. The studied CoFeB thickness range is much larger than the typical FM layer thickness where field-like torque-induced artifact is important (e.g., t_F ~ 3 nm for Pt/CoFe). Hence, the large ξ_{FMR} in the thick FM layer reflects the high torque efficiency. Identical experiments were carried out in NiFe(t)/Ru(6)/Al_2O_3(2) control samples, yielding ξ_{FMR} and $4\pi M_{eff}$ [Fig. 3.2(c)]. The torque efficiency keeps a value of ξ_{FMR} as small as ~ 0.03 for all NiFe thicknesses.

Depending on the selection of FM materials (CoFeB and NiFe with different value of $\eta_{L\text{-}S}$), the OT magntidue and the OT dependency on the FM thickness completely changes, revealing the unique feature of OT. In conventional spin-orbit torque and other interfacial torque mechanisms, such as anomalous spin-orbit torque, the torque efficieny is constant with the change of the FM thickness. The different FM thickness dependence between OT and other torques would be understood by the different role of FM as an aspect of the torque generation [Fig. 2(e)]: For the former, the angular momentum transfer between the orbital current and the magnetization is mediated by the SOC. In contrast, for the latter, the angular momentum transfer between the spin current and the magnetization is based on the *s*-*d* exchange interaction. Since the SOC is much smaller than the *s*-*d* exchange interaction, the orbital current can propagate a long distance in FM. Note that a recent Rashba-Edelstein magnetoresistance experiment reported similar ferromagnet thickness dependent behavior due to the characteristic orbital transport [16]. In comparison, spin current dephasing occurs rapidly in the FM due to the strong *s*-*d* exchange interaction, thus the propagation length is much shorter. We believe such a long propagation length and FM-thickness beneficial characteristic ensure that orbital torque is favorable for the memories and magnetic sensor applications.

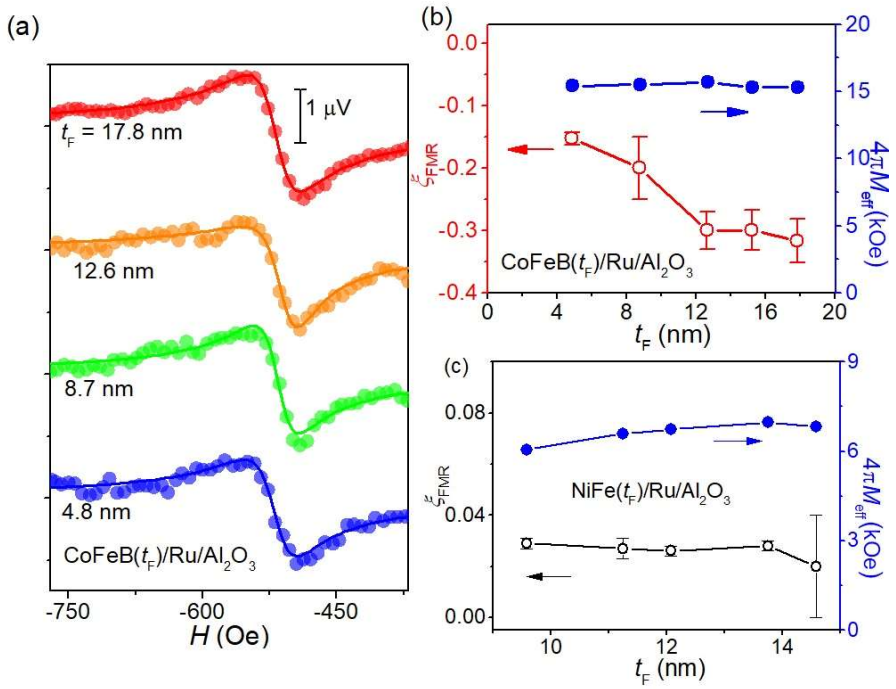

Fig. 3.2. (a) ST-FMR spectra of CoFeB(t)/Ru(6)/Al_2O_3(2) devices with different CoFeB thicknesses. (b) Ferromagnetic thickness dependence of the ξ_{FMR} and $4\pi M_{eff}$ of CoFeB(t_F)/Ru(6)/Al_2O_3(2). (c) ξ_{FMR} and $4\pi M_{eff}$ of NiFe(t_F)/Ru(6)/Al_2O_3(2) as a function of ferromagnetic layer thickness. (d) (e) Schematic of the angular momentum current-to-spin torque conversion processes of OT and spin-orbit torque in the ferromagnetic metal.

3.3 Artifact exclusion

In this section, we will discuss the field-like torque contribution in the ST-FMR measurement, and compare the ST-FMR results and the USMR results, to confirm the correctness of the the analysis based on the ST-FMR results. Taking the field-like torque into account, the ST-FMR signal is given by

$$S = -\frac{1}{4}\frac{dR}{d\varphi}\frac{\gamma I_{rf}\cos\varphi}{\Delta 2\pi(df/dH)|_{H_{ext}=H_0}}\frac{\hbar}{2e}\frac{\xi_{DL}}{4\pi M_s t_F}, \quad (3\text{-}1)$$

$$A = -\frac{1}{4}\frac{dR}{d\varphi}\frac{\gamma I_{rf}\cos\varphi}{\Delta 2\pi(df/dH)|_{H_{ext}=H_0}}\left[\frac{\hbar}{2e}\frac{\xi_{FL}}{4\pi M_s t_F}+\frac{J_c t_{Ru}}{2}\right]\sqrt{1+\frac{4\pi M_{eff}}{H_0}}, \quad (3\text{-}2)$$

where ξ_{DL} and ξ_{FL} are the torque efficiencies of damping-like and filed-like torque, respectively. When both torque efficiencies are constant, the CoFeB thickness t_F dependence of ξ_{FMR} would be given by

$$\frac{1}{\xi_{FMR}} = \frac{1}{\xi_{DL}}\left(1+\frac{\hbar}{e}\frac{\xi_{FL}}{4\pi M_s t_F t_{Ru}}\right). \quad (3\text{-}3)$$

Fitting using (3-3) is shown in Fig. 3.3, which yields $\xi_{DL} = -0.55$ and $\xi_{FL} = 4.25$. This ξ_{FL} is two orders larger than the values in previously reported systems with large field-like torque effect [22,23]. Therefore, the strong CoFeB thickness dependence of ξ_{FMR} is unlikely to be caused by a constant field-like torque.

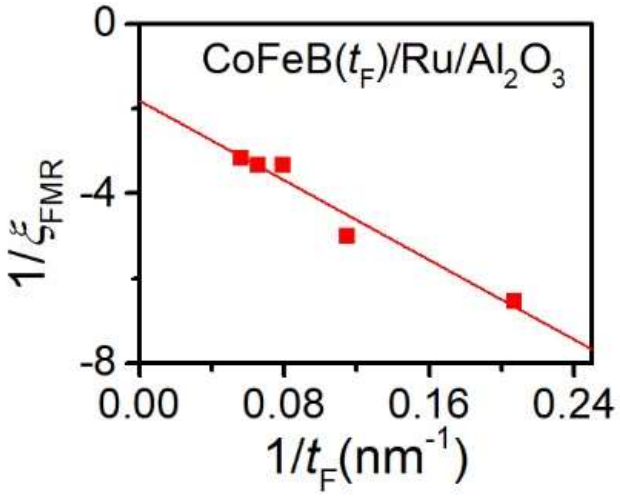

Fig.3.3. Fitting of the CoFeB thickness-dependent ξ_{FMR} using Eq. (S3).

We carried out the USMR measurement for CoFeB(12.2)/Ru(6)/Al_2O_3(2) stack with a thick CoFeB layer [Fig. 3.4]. The USMR and the thermal effects can generate the second harmonic longitudinal resistance signal R_{xx} 2ω. We carefully consider the thermal contribution and eventually obtain a pure USMR signal $\Delta R_{USMR}/R = 1.1 \times 10^{-5}$ at a current density of 1.7×10^6 A cm^{-2}, which is larger than the USMR signal in Pt/Co, Ta/Co, and NiFe/Oxidized Cu. This large USMR can be understood as the generation of the substantial orbital torque, as shown in Fig. 3.2(b). After subtracting it from the second-harmonic R_{xx} signal under β rotation, we obtain the pure USMR signal $\Delta R_{USMR}/R = 1.1 \times 10^{-5}$ at a current density of 1.74×10^6 A/cm^2, which is larger than the USMR signal in Pt/Co [21], Ta/Co [21] and NiFe/Oxidized Cu [24].

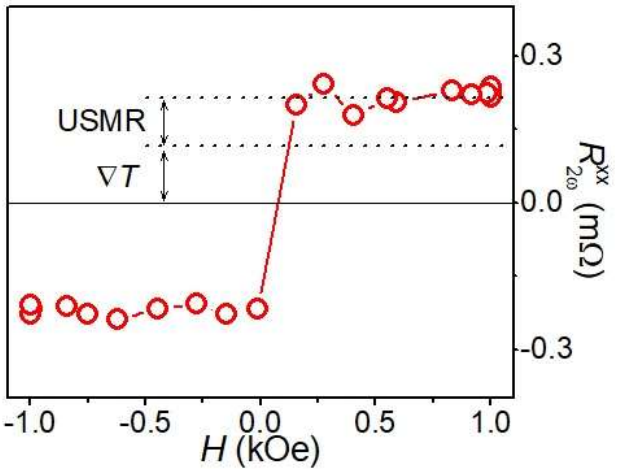

Fig. 3.4 USMR signal of CoFeB(12.2)/Ru(6)/Al_2O_3(2) at current density 1.7×10^6 A cm^{-2}. ∇T represents the thermal contrivution to the second harmonic signal.

Here we briefly discuss the large USMR effect observed in the CoFeB(12.6)/Ru(7)/Al_2O_3(2) stack. In general, the USMR can be explained by the difference of the conductivity between majority and minority spins,We note that the number of the majority and minority spin is represented by the nonequilibrium spin accumulation δs. And δs is evaluated by a relation $\tau \sim \delta s/t$, where τ is the spin torque, and t is the spin relaxation time in the FM. If we utilize τ from the ST-FMR measurement, we could obtain the difference of conductivity by following,

$$\Delta\sigma = \frac{\delta s}{\hbar(n_\uparrow + n_\downarrow)}(\sigma_\uparrow - \sigma_\downarrow), \quad (3\text{-}4)$$

where $n_\uparrow$ and $n_\downarrow$ are the Fermi level density of states of the majority spins and minority spins of the ferromagnetic layer, respectively, $\sigma_\uparrow$ and $\sigma_\downarrow$ are the conductivity of the majority spins and minority spins, respectively. The USMR is given by

$$\mathrm{USMR} = \frac{\Delta\sigma}{\sigma_0 + \sigma_N}, \quad (3\text{-}5)$$

where σ_N is the conductivity of the Ru layer, and σ_0 is the conductivity of the CoFeB layer given by

$$\sigma_0 = \frac{n_\uparrow\sigma_\uparrow + n_\downarrow\sigma_\downarrow}{n_\uparrow + n_\downarrow}. \quad (3\text{-}6)$$

Taking the current-induced torque efficiency $j_s/j_C = 0.3$, spin relaxation time $t = 1\times10^{-13}$s, $n_\uparrow + n_\downarrow = 1\times10^{16}$ cm^{-2}, $(n_\uparrow + n_\downarrow)(\sigma_\uparrow - \sigma_\downarrow)/(n_\uparrow\sigma_\uparrow + n_\downarrow\sigma_\downarrow) = 1.2$, the USMR signal is estimated to be ~ 1×10^{-5} for current density 1.74×10^6 A/cm^2. It is same order of magnitude with the experimental result.

3.4 Ru thickness dependence

We now turn towards the Ru thickness-dependent orbital torque effect. CoFeB is fixed to 7 nm for this experiment. Fig. 3.5(a) shows evaluated ξ_{FMR} as a function of Ru thickness in CoFeB(7)/Ru(t)/'Al_2O_3(2) stack. Remarkably, the absolute value of ξ_{FMR} turns out small ($|\xi_{FMR}| = 0.05$) for $t_{Ru} = 2$ nm, but it enhances with increasing the Ru thickness. When $t_{Ru} = 7$ nm, $|\xi_{FMR}|$ reaches a maximum of 0.18; further increase in t_{Ru} makes $|\xi_{FMR}|$ decrease. Measurements of the Ru thickness dependence of OT is performed for NiFe(7)/Pt(1)/Ru(t_{Ru})/Al_2O_3(2) and NiFe(7)/Ru(t_{Ru})/Al_2O_3(2) stacks [Fig. 3.5(b)]. Similar to the OT in the stack with FM=CoFeB, ξ_{FMR} increases with increasing t_{Ru} for $t_{Ru} < 6$ nm, and decreases when $t_{Ru} > 7$ nm in the NiFe(7)/Pt(1)/Ru(t_{Ru})/Al_2O_3(2) stack. The decreasing $|\xi_{FMR}|$ suggests that an orbital relaxation process reduces the OT in the thick Ru layer, which is distinct from the OT purely coming from the bulk. Hence, the ORE from the Ru/Al_2O_3 interface contributes importantly to the observed large torque effect in the CoFeB/Ru/Al_2O_3 stack. The much smaller torque effect at small t_{Ru} demonstrates that the ORE contribution is also smaller with ultrathin Ru layer, which can be ascribed to the degradation of material quality (roughness, crystalline quality, etc.) of the Ru/Al_2O_3 interface. Contrast to above results, ξ_{FMR} exhibits no obvious t_{Ru} dependence in the NiFe(7)/Ru(t_{Ru})/Al_2O_3(2) stack. Nearly constant ξ_{FMR} for this stack is consistent with the small $\eta_{L\text{-}S}$ in NiFe. We note that, unfortunately, we cannot obtain clear ST-FMR signal for samples with the thick Ru thickness due to the small anisotropic magnetoresistance of CoFeB and the current shunting effect in Ru layer. The orbital Hall effect in Ru may also contribute to the torque effect, but cannot explain the decreasing OT efficiency in the thick Ru regime, and thus cannot be the origin of the thickness dependent behavior. Using other kinds of ferromagnets with both large SOC and anisotropic magnetoresistance for thicker Ru may help to further quantify the the contributions of ORE and OHE, but is beyond the scope of the present work.

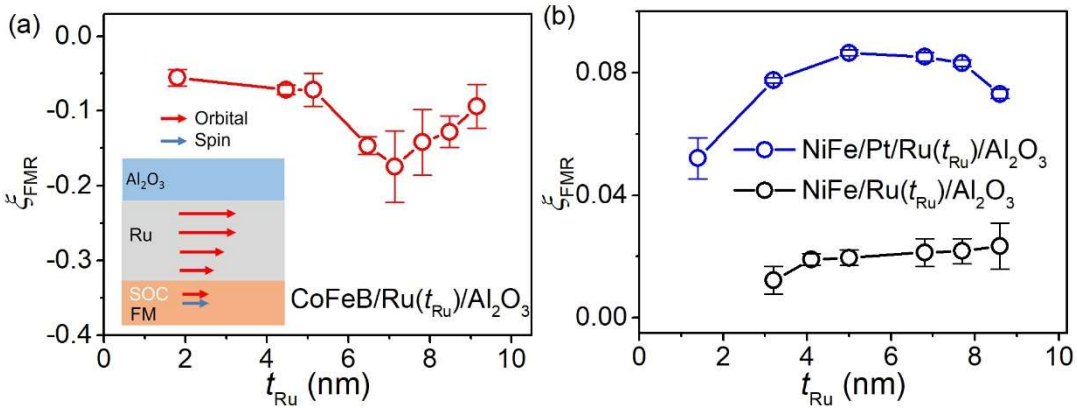

Fig. 3.5. t_{Ru} dependence of the calculated ξ_{FMR} of (a) CoFeB(7)/Ru(t_{Ru})/Al_2O_3(2), (b) NiFe(7)/Ru(t_{Ru})/Al_2O_3(2) (black circles) and NiFe(7)/Pt(1)/Ru(t_{Ru})/Al_2O_3(2) (blue circles). The inset of (a) is the schematic illustration of the orbital current propagating across the Ru layer, converted to the torque via SOC.

4. Theory

4.1 Orbital Rashba effect

We theoretically consider the orbital generation and transport in the Ru/Al_2O_3 polycrystalline structure. The generation of the orbital current due to ORE requires interfacial orbital hybridization, which can survive in polycrystalline interfaces as evidenced by the orbital reconstruction-induced voltage control magnetic anisotropy effect in polycrystalline stacks [25,26]. Hence, we develop two tight-binding models on the simple square and diamond lattices, which are typical two-dimensional lattices. The orbital Rashba effect is then estimated with the methods developed by Go et al. [11].

In our measurement geometric, the current is along x direction and the orbital/spin polarization are along y direction. We consider the d_{xz}, d_{yz}, d_{xy} orbits in the Ru 4*d* states, which hybridized with the p_x, p_y orbits in the O 2*p* states. The p_z orbit is not considered because the rotational symmetry prohibits the hybridization between it and the Ru 4d states. The *d* orbitals distribute between –0.1 to 0.2 eV. The superposition $d_{yz} \pm id_{xy}$ can carry orbital angular momenta in y direction. Although the direct

hopping between the two orbits are prohibited by symmetry, the coupling between them could be mediated by the p_y orbit in the O 2p states at the interface, since the different position of the Ru and O atoms allow the $d_{yz} - p_y$ and the $d_{xy} - p_y$ hybridizations. In a square Brillouin zone as shown in Fig. 4.1(a), the model Hamiltonian can be written as

$$H = \begin{pmatrix} E_{dxz}(k_x,k_y) & 0 & 0 & \alpha & 0 \\ 0 & E_{dyz}(k_x,k_y) & 0 & 0 & \alpha \\ 0 & 0 & E_{dxy}(k_x,k_y) & i\beta\sin(k_y a) & i\beta\sin(k_x a) \\ \alpha & 0 & -i\beta\sin(k_y a) & E_p & 0 \\ 0 & \alpha & -i\beta\sin(k_x a) & 0 & E_p \end{pmatrix}, \quad (4\text{-}1)$$

where a is the lattice constant, α and β are coupling parameters, E_p is the onsite energy of the p_y orbit of the O atoms. The energy of the d_{yz} and d_{xy} orbits are given by

$$\begin{aligned} E_{dxz}(k_x,k_y) &= E_d + \Delta + 2t_\pi\cos(k_x a) - 2t_\delta\cos(k_y a), \\ E_{dyz}(k_x,k_y) &= E_d + \Delta + 2t_\pi\cos(k_y a) - 2t_\delta\cos(k_x a), \quad (4\text{-}2) \\ E_{dxy}(k_x,k_y) &= E_d - \Delta + 2t_\pi\cos(k_x a) + 2t_\pi\cos(k_y a), \end{aligned}$$

where E_d is the onsite energy for d electrons, Δ is the crystal field splitting, t_π and t_δ are the hopping parameters of π and δ bonds, respectively. Using $E_d = 0$, $E_p = -0.5$ eV, $\Delta = 0.1$ eV, $t_\pi = 0.05$ eV, $t_\delta = 0.025$ eV, $\alpha = 0.07$ eV, $\beta = 0.025$ eV, the band dispersion is obtained as shown in Fig. 4.1(b), where the two higher energy bands come from the Ru 4d states and the lower energy one comes from the O 2p states. In a diamond lattice [Fig. 4.1(c)], (4-2) should be replaced by

$$\begin{aligned} E_{dxz}(k_x,k_y) &= E_d + \Delta - 4t_1\cos(\frac{1}{2}k_x a)\cos(\frac{\sqrt{3}}{2}k_y a) - 2t_\delta\cos(k_x a), \\ E_{dyz}(k_x,k_y) &= E_d + \Delta - 4t_1\cos(\frac{1}{2}k_x a)\cos(\frac{\sqrt{3}}{2}k_y a) + 2t_\pi\cos(k_x a), \quad (4\text{-}3) \\ E_{dxy}(k_x,k_y) &= E_d - \Delta + 2t_\pi\cos(k_x a) + 4t_2\cos(\frac{1}{2}k_x a)\cos(\frac{\sqrt{3}}{2}k_y a), \end{aligned}$$

where $t_1 = 0.02$eV and $t_2 = 0.03$eV are the hopping parameters of tilted bonds for out-of-plane and in-plane orbits, respectively. The band dispersion is obtained with other parameters like the square lattice case, as shown in Fig. 4.1(d).

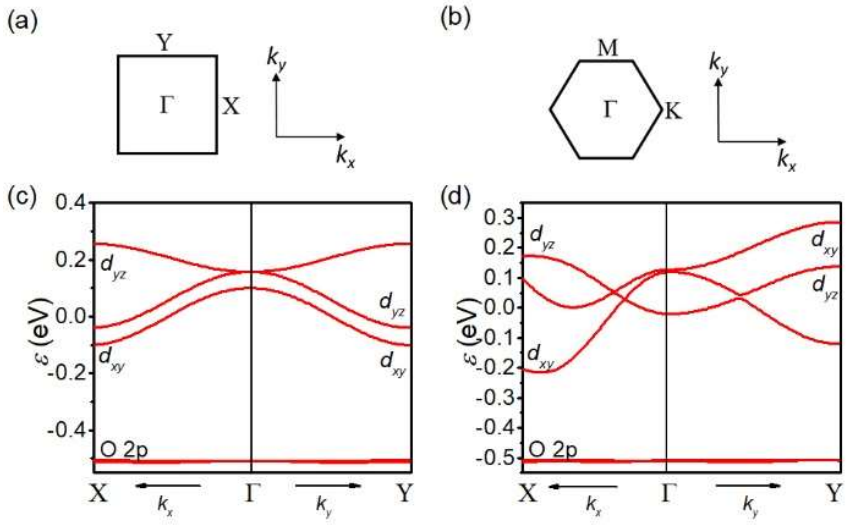

Fig.4.1. model for the Orbital Rashba effect. (a) and (b) are the Brillouin zone for the minimum model of square and diamond lattices, respectively. (c) and (d) are the band dispersion of square and diamond lattices, respectively.

We can calculate the strength of the orbital Rashba effect using the Kubo formula

$$\left\langle \delta L_y \right\rangle = \frac{e\hbar E_x}{2\Gamma} \sum_n \int \frac{d^2k}{(2\pi)^2} f_{nk}' \left\langle u_{nk} \left| L_y \right| u_{nk} \right\rangle \left\langle u_{nk} \left| v_x \right| u_{nk} \right\rangle, \quad (4\text{-}4)$$

where L_y is the angular momentum operator in the y direction, $|u_{nk}\rangle$ is the periodic part of the Bloch wave function with band index n and wave vector k, f_{nk} is the corresponding Fermi-Dirac distribution function, E_x is the electric field at the x direction, v_x is the velocity operator at the x direction, Γ is quasi-particle relaxation rate. To compare the theoretical model with the experimental results, the effective orbital Hall conductivity can be estimated with $(\delta L/E)\cdot v_F/a^3$, where v_F is the Fermi velocity. Γ = 0.025 eV is taken for k_BT at room temperature [4], where k_B is the Boltzmann constant. For typical elemental metal, the Fermi velocity is at the order of 10^6 m/s, and lattice constant a is several Å. Using these values, we obtain the effective orbital Hall conductivity is at the order of 10^3 to 10^4 $(\hbar/2e)$ $\Omega^{-1}\cdot cm^{-1}$ (Fig. 4.2), at the same order as the experimental value.

As illustrated in Fig. 4.2, ORE in the square and diamond lattices show the same sign and similar Fermi level dependence. When the d bands are filled (E_F > 0.3 eV), $\delta L/E$ is almost zero. $\delta L/E$ starts to increase when E_F moves towards the middle point of the d bands and reaches a maximum near E_F = 0. When E_F further decreases, $\delta L/E$ starts to drop. The Fermi level dependence reveals that partially filled d electrons are

critical for the orbital generation, while the crystal orientation just provides a negligible effect. Notably, the chiral orbital texture depends only on the energy difference between the Ru *d* and the O 2*p* states. It would not be influenced by the crystal orientation, making the survival of the ORE in the polycrystalline samples.

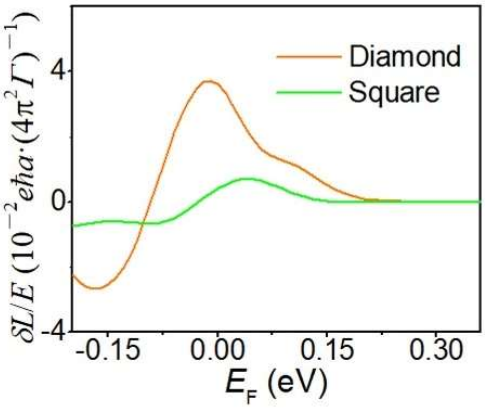

Fig. 4.2 Fermi level dependence of the ORE.

We now analyze the obtained OT efficiency and propose models for the orbital current generation. The observed maximum torque efficiency is 0.3, taking the resistivity of the Ru film ~ 50 μΩ·cm into account, the effective orbital Hall conductivity is estimated to be ~ 6×10^3 $(\hbar/2e)$ $\Omega^{-1}\cdot cm^{-1}$, much larger than that of heavy metal Pt [2,27] and W [28], and most of the topological insulators [29,30].

4.2 Orbital hopping model

The ORE at the polycrystalline Ru/Al_2O_3 interface corresponds to average of several single crystals with different orientations. The propagation of orbital current in polycrystalline structures become greatly different to that in single crystalline structures. Single crystalline structures with orbital degeneracy provide a long lifetime for the orbital superposition state. However, a crystal field splitting Δ of the orbitals in the single crystalline structures would drive the orbital superposition states into oscillation. It makes a relaxation of orbital current during the time of $t_1 \sim \hbar/\Delta$. On the other hand, in polycrystalline samples, if the crystal field Δ is random, the electrons carrying the orbital angular momentum could meet both positive and negative oscillation which would provide cancelling out. This cancellation leads to a

counterintuitive result; with the same crystal field Δ, polycrystalline structures are more favorable for the orbital transport than single crystalline structures.

We now use the quantum evolution equation $|\psi(t+\delta t)\rangle = exp(-i\frac{\hat{H}}{\hbar}\delta t)|\psi(t)\rangle$ on a one-dimensional (1D) atom chain to calculate the orbital transport in the single crystalline and polycrystalline structures. A $t = 0$ state with an electron with a wave function $|\psi_0\rangle = \frac{1}{\sqrt{2}}(d_{yz} - id_{xy})$, which corresponds to $L_y = \hbar$ for a first atom but empty state for all other orbitals.

In the simulation, the Hamiltonian consists of the crystal field and hopping terms. The crystal field of the first atom (atom 1) and the last atom (atom l) are set to be 0 to eliminate the oscillation at the boundary and emphasize the transport-related behavior. Except these two atoms, the crystal field has the same finite value Δ in all other atoms in the middle (atom 2 to atom $l - 1$) for the uniform crystal field case [Fig. 4.3 upper panel], and has evenly distributed random values in [–Δ, Δ] for the random crystal field case [Fig. 4.3 lower panel].

The hopping terms include the hopping between the same orbital and the inter-orbital hopping. A hopping energy $J = 0.3$ eV is used between the same orbitals of nearest atoms. Set the direction of the chain as x direction, the hopping between different orbitals of nearest atoms are forbidden in single crystal chains due to the xy and xz mirror symmetry. Considering the inter-orbital hopping between two nearest atoms, when they only have difference in y or z coordinate, the xy or xz mirror symmetry still exists, respectively, and the inter-orbital hopping is still prevented. Only when the coordinates of the two atoms (x_i, y_i, z_i) and (x_j, y_j, z_j) have different y and z values at the same time, i.e., $y_i \neq y_j$ and $z_i \neq z_j$, can the inter-orbital hopping happen. Such hopping is usually small when the position derivation $|y_i - y_j|$ and $|z_i - z_j|$ are not large. The hopping integral has two-fold symmetry around the x axis, the same as the crystal field, and has maximum value when $|y_i - y_j| = |z_i - z_j|$ for a given derivation distance $r = ((y_i - y_j)^2+(z_i - z_j)^2)^{1/2}$. This condition corresponds to a 45° derivation. Meanwhile, since the positive and negative crystal field can be regarded as in-plane and out-of-plane orientations connected by a 90° rotation, an atom with zero crystal field can be approximately regarded as having experienced a near 45° rotation. Therefore, a simple estimation of the inter-orbital hopping term J' between atom i and j is $J'_{ij} = \lambda J(\Delta_i - \Delta_j)/\Delta$, where Δ is the maximum crystal field, Δ_i is the crystal field at the atom i, $J = 0.3$ eV is the hopping term between the same orbital, and λ is a random

parameter distributes between – 0.2 and 0.2 evenly. Here the $(\Delta_i - \Delta_j)/\Delta$ term describes the direction of the derivation between atom i and j, and λ describes the amplitude of the derivation.

Note that the model for the random crystal field is suitable for polycrystalline structures with small grain size. Considering that the grain size of the Ru layer is less than 10 nm as supported by the absence of a clear grain in the high-resolution transmission electron microscope observation (Fig. 2.2), condition of the stacks in this study is well fitted with the above model.

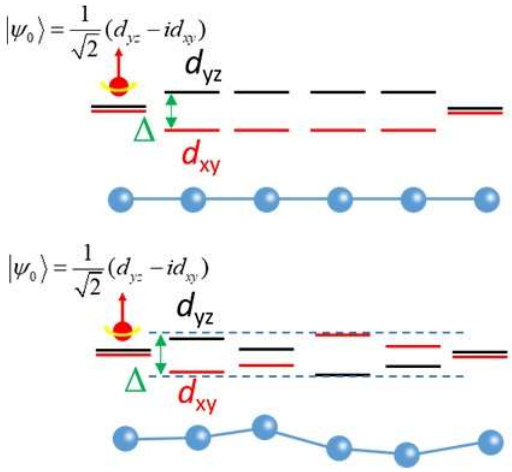

Fig. 4.3 Schematics of 1D atom chain with uniform crystal field and random crystal field in bulk. The crystal fields of the first and the last atom are set to be 0.

Fig. 4.4(a) displays the time evolution of the orbital angular momentum at the first and the last atoms in an $l = 9$, 1D atom chain with uniform crystal field $\Delta = 0.1$ eV. At $t = 0$, atom 1 has $L_y = \hbar$ and atom 9 has $L_y = 0$. Then L_y of atom 1 decreases due to the electron hopping, and the orbital angular momentum is transferred to the atoms in the middle. When t =20 $\hbar$/eV, the electron wave function reaches atom 9, carrying the orbital angular momentum –0.6$\hbar$. The negative sign reveals that the crystal field-induced orbital oscillation accumulates during the transport, and the orbital angular momentum is switched from the initial state. In contrast, under a random crystal field [Fig. 4.4(b)], the L_y peak value is 0.6 $\hbar$ at $t \sim 20$ $\hbar$/eV, with the same sign as the initial orbital angular momentum due to the compensation of the different oscillation directions at different atoms. To analyze the orbital transport efficiency, we evaluate the positive and negative maximum L_y on the last atom, labeled as L_M and L_m,

respectively, from $t = 0$ to $t = 80$ $\hbar$/eV. Usually, one of L_M and L_m is the L_y peak due to orbital transport, and the other represents the random orbital fluctuation amplitude. Hence ($L_M + L_m$) is selected as the figure of merit of the orbital transport. We numerically calculate atom chains with atom number $l = 5$ to 15 and $\Delta = 0$, 0.05, 0.1 and 0.2 eV. Data points are collected from an average of 200 times simulations to calculate the random crystal field condition. As shown in Fig. 4(c), the strongest orbital transport is shown for $\Delta = 0$ with a uniform crystal field. In the uniform crystal field condition, the positive–negative–positive orbital oscillation starts to be driven when Δ=0.05 eV and the similar behavior persists for Δ>0.05 eV.

At $\Delta = 0$, due to the orbital mixing hopping J', the orbital transport is less efficient when the crystal field is random [Fig. 4.4(d)]. However, as Δ increases, the orbital transport is maintained without oscillation, although the decay of the orbital angular moment is not negligible. Hence, we conclude that long-range orbital transport can occur in the random crystal field case if the crystal field is smaller than the hopping energy. In contrast, a uniform crystal field with the same magnitude can quickly destroy the orbital transport. Although the band dispersion and filling in actual samples can lead to more complicated crystal field dependence of the orbital transport, the 1D model captures the key point of the different orbital oscillation behavior between uniform and random crystal fields, which should appear in the actual samples in complex condition. Thus, this model indicates that polycrystalline structures are possibly more efficient for some materials with crystal fields than single crystalline structures.

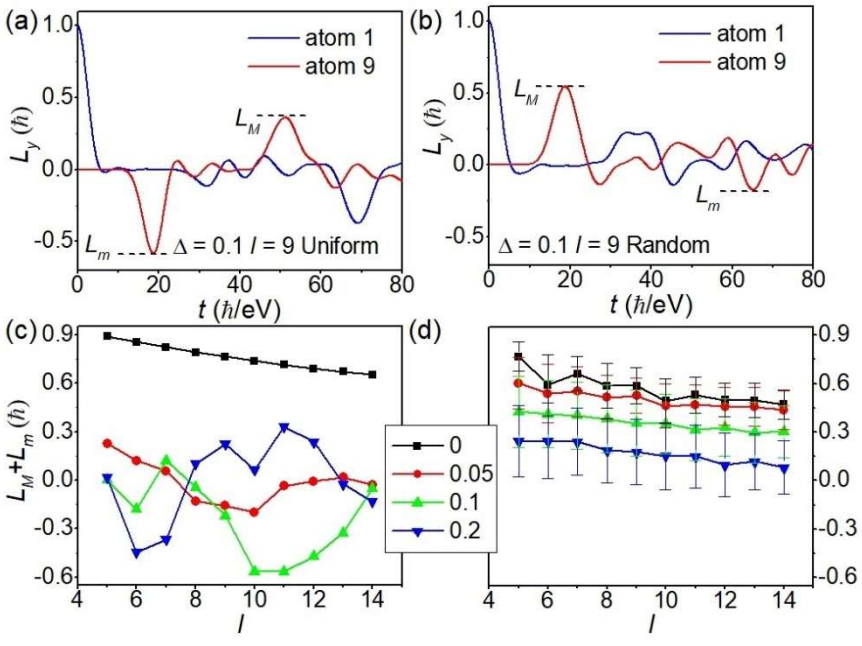

Fig. 4.4. (a) and (b) are the time evolution of the orbital angular momentum L_y in the uniform and random crystal field atom chains, respectively. The blue curve represents the L_y at the first atom (atom 1), and the red curve represents the L_y at the last atom (atom 9), with crystal field $V = 0.1$ eV and the atom number $l = 9$. The positive and negative maximum L_y are labeled as L_M and L_m, respectively. (c) and (d) are the atom number l dependence of $L_M + L_m$ with uniform and random crystal field, respectively, and crystal field magnitude $V = 0$ (black), 0.05 eV (red), 0.1 eV (green) and 0.2 eV (blue). Data points for the random crystal field are obtained from 200 simulations, and the error bar is the corresponding standard derivation.

5. Conclusion

In conclusion, we have demonstrated a remarkable OT effect in the polycrystalline FM/Ru/Al_2O_3 stack, mediated by the efficient long-range orbital transport in the uniform polycrystalline Ru layer. We find characteristic behaviors of OT; (i) the sign and magnitude of the torque efficiency are strongly dependent on the FM materials and insertion layers according to the sign and magnitude of their SOC, and (ii) the torque efficiency is enhanced with increasing CoFeB layer thickness t_F, with a large saturation torque efficiency 0.3 for t_F = 12 nm, consistent with the long propagation length of the orbital current in the ferromagnet. The torque efficiency reaches the maximum value at the Ru layer thickness of 7 nm. It decreases with Ru layer thickness, revealing the ORE at the Ru/Al_2O_3 interface as the origin of the orbital current. The tight-binding model with different crystal structures shows that ORE can maintain at polycrystalline interfaces. Our quantum evolution simulation shows the unique random processing feature of the orbital transport in the polycrystalline materials, which enables long-range orbital transport in polycrystalline samples even in the presence of a crystal field. Our results show that transition-metal-based materials with small SOC, simple crystal structure and itinerant *d* electrons can provide a suitable platform for studying orbital transport and developing devices.

Publication

L. Y. Liao*, F. H. Xue*, L. Han, J. Kim, R. Q. Zhang, L. Li, J. M. Liu, X. F. Kou, C. Song, F. Pan, and Y. Otani, Efficient orbital torque in polycrystalline ferromagnetic-metal/Ru/Al_2O_3 stacks: Theory and experiment, Phys. Rev. B 105, 104434 (2022).

Acknowledgement

I would like to give my acknowledgement to everyone who helped me during my Master study. First of all, I would like to express my sincere thanks to my supervisor, Prof. Yoshichika Otani, in the Institute for Solid State Physics at the University of Tokyo, for giving me the chance to study in the group, providing insightful guidance and supporting my research. Prof. Otani has a profound understanding of science and a firm attitude toward pursuing the truth, which are great driving forces for me to keep moving forward on the road of research.

I would also like to thank Dr. Junyeon Kim in RIKEN for his valuable discussion and suggestion during my research and thesis writing. Due to the pandemic, I could not come to Japan nearly until the end of my Master course period, and I luckily got the opportunity to finish my experiment in China with the help of Prof. Cheng Song at Tsinghua University and Prof. Xufeng Kou at ShanghaiTech University. Without their support, I cannot advance my research and finish this thesis.

I appreciate Dr. Kouta Kondou, Dr. Jorge Puebla, Dr. Tomas Lyons in RIKEN, and Dr. Hironari Isshiki at the University of Tokyo for teaching me a lot of knowledge about experiments and physics.

I’m grateful to Mr. Lei Han, Ms. Ruiqi Zhang, Mr. Xingshuai He, and Mr. Tongjin Chen at Tsinghua University, Dr. Lu Sun, and Mr. Fenghua Xue at ShanghaiTech University for their kind help in my experiment.

Dr. Mingran Xu, Mr. Yunyoung Hwang, Mr. Mingxing Wu, Mr. Handa Wang in RIKEN, and Dr. Ayuko Kobayashi at the University of Tokyo also helped me a lot from science to life in Japan. During my time in China, I worked and learned together with Dr. Lin Huang, Mr. Yongjian Zhou, Ms. Leilei Qiao, Mr. Ruyi Chen, Mr. Wenxuan Zhu, Mr. Hua Bai, Mr. Qian Wang, Mr. Zhiyuan Zhou, Mr. Chong Chen, Mr. Yichen Su, Mr. Tingwen Guo, Ms. Shixuan Liang in Tsinghua University, Mr. Lun Li, Mr. Jiuming Liu, and Mr. Yong Zhang in ShanghaiTech University. It is a great pleasure to work with all of them. I also need to thank our group secretary Ms. Michiko Ishinabe, Ms. Yoko Kaneda, and Ms. Tomoko Kobayashi, for their helpful work.

Finally, I would like to thank my family for their support and understanding of my research life.

Reference

[1] I. M. Miron, K. Garello, G. Gaudin, P. J. Zermatten, M. v. Costache, S. Auffret, S. Bandiera, B. Rodmacq, A. Schuhl, and P. Gambardella, *Perpendicular Switching of a Single Ferromagnetic Layer Induced by In-Plane Current Injection*, Nature **476**, 189 (2011).

[2] L. Liu, C.-F. Pai, Y. Li, H. W. Tseng, D. C. Ralph, and R. A. Buhrman, *Spin-Torque Switching with the Giant Spin Hall Effect of Tantalum*, Science **336**, 555 (2012).

[3] D. Lee et al., *Orbital Torque in Magnetic Bilayers*, Nature Communications **12**, 6710 (2021).

[4] J. Kim, D. Go, H. Tsai, D. Jo, K. Kondou, H. W. Lee, and Y. Otani, *Nontrivial Torque Generation by Orbital Angular Momentum Injection in Ferromagnetic-Metal/ Cu/Al2O3 Trilayers*, Physical Review B **103**, L020407 (2021).

[5] X. Chen, Y. Liu, G. Yang, H. Shi, C. Hu, M. Li, and H. Zeng, *Giant Antidamping Orbital Torque Originating from the Orbital Rashba-Edelstein Effect in Ferromagnetic Heterostructures*, Nature Communications **9**, 2569 (2018).

[6] Y. Tazaki, Y. Kageyama, H. Hayashi, T. Harumoto, T. Gao, J. Shi, and K. Ando, *Current-Induced Torque Originating from Orbital Current*, arXiv:2004.09165.

[7] S. Lee et al., *Efficient Conversion of Orbital Hall Current to Spin Current for Spin-Orbit Torque Switching*, Communication Physics **4**, 234 (2021).

[8] S. Ding et al., *Harnessing Orbital-to-Spin Conversion of Interfacial Orbital Currents for Efficient Spin-Orbit Torques*, Physical Review Letters **125**, 177201 (2020).

[9] D. Go, D. Jo, C. Kim, and H. W. Lee, *Intrinsic Spin and Orbital Hall Effects from Orbital Texture*, Physical Review Letters **121**, 086602 (2018).

[10] H. Kontani, T. Tanaka, D. S. Hirashima, K. Yamada, and J. Inoue, *Giant Orbital Hall Effect in Transition Metals: Origin of Large Spin and Anomalous Hall Effects*, Physical Review Letters **102**, 016601 (2009).

[11] D. Go, D. Jo, T. Gao, K. Ando, S. Blügel, H. W. Lee, and Y. Mokrousov, *Orbital Rashba Effect in a Surface-Oxidized Cu Film*, Physical Review B **103**, L121113 (2021).

[12] S. R. Park, C. H. Kim, J. Yu, J. H. Han, and C. Kim, *Orbital-Angular-Momentum Based Origin of Rashba-Type Surface Band Splitting*, Physical Review Letters **107**, 156803 (2011).

[13] D. Go, D. Jo, H. W. Lee, M. Kläui, and Y. Mokrousov, *Orbitronics: Orbital Currents in Solids*, EPL **135**, 37001 (2021).

[14] D. Jo, D. Go, and H. W. Lee, *Gigantic Intrinsic Orbital Hall Effects in Weakly Spin-Orbit Coupled Metals*, Physical Review B **98**, 214405 (2018).

[15] D. Go, D. Jo, K.-W. Kim, S. Lee, M.-G. Kang, B.-G. Park, S. Blügel, H.-W. Lee, and Y. Mokrousov, *Long-Range Orbital Magnetoelectric Torque in Ferromagnets*, ArXiv:2106.07928.

[16] S. Ding et al., *Observation of the Orbital Rashba-Edelstein Magnetoresistance*, Physical Review Letters **128**, 067201 (2022).

[17] H. An, Y. Kageyama, Y. Kanno, N. Enishi, and K. Ando, *Spin-Torque Generator Engineered by Natural Oxidation of Cu*, Nature Communications **7**, 13069 (2016).

[18] Z. Wen, J. Kim, H. Sukegawa, M. Hayashi, and S. Mitani, *Spin-Orbit Torque in Cr/CoFeAl/MgO and Ru/CoFeAl/MgO Epitaxial Magnetic Heterostructures*, AIP Advances **6**, 056307 (2016).

[19] K. Kondou, H. Sukegawa, S. Kasai, S. Mitani, Y. Niimi, and Y. Otani, *Influence of Inverse Spin Hall Effect in Spin-Torque Ferromagnetic Resonance Measurements*, Applied Physics Express **9**, 023002 (2016).

[20] H. Nakayama et al., *Spin Hall Magnetoresistance Induced by a Nonequilibrium Proximity Effect*, Physical Review Letters **110**, 206601 (2013).

[21] C. O. Avci, K. Garello, A. Ghosh, M. Gabureac, S. F. Alvarado, and P. Gambardella, *Unidirectional Spin Hall Magnetoresistance in Ferromagnet/Normal Metal Bilayers*, Nature Physics **11**, 570 (2015).

[22] C. F. Pai, Y. Ou, L. H. Vilela-Leão, D. C. Ralph, and R. A. Buhrman, *Dependence of the Efficiency of Spin Hall Torque on the Transparency of Pt/Ferromagnetic Layer Interfaces*, Physical Review B **92**, 064426 (2015).

[23] S. Emori, T. Nan, A. M. Belkessam, X. Wang, A. D. Matyushov, C. J. Babroski, Y. Gao, H. Lin, and N. X. Sun, *Interfacial Spin-Orbit Torque without Bulk Spin-Orbit Coupling*, Physical Review B **93**, 180402(R) (2016).

[24] G. Okano, M. Matsuo, Y. Ohnuma, S. Maekawa, and Y. Nozaki, *Nonreciprocal Spin Current Generation in Surface-Oxidized Copper Films*, Physical Review Letters **122**, 217701 (2019).

[25] T. Nozaki, Y. Shiota, M. Shiraishi, T. Shinjo, and Y. Suzuki, *Voltage-Induced Perpendicular Magnetic Anisotropy Change in Magnetic Tunnel Junctions*, Applied Physics Letters **96**, 022506 (2010).

[26] W. G. Wang, M. Li, S. Hageman, and C. L. Chien, *Electric-Field-Assisted Switching in Magnetic Tunneljunctions*, Nature Materials **11**, 64 (2012).

[27] G. Y. Guo, S. Maekawa, and N. Nagaosa, *Enhanced Spin Hall Effect by Resonant Skew Scattering in the Orbital-Dependent Kondo Effect*, Physical Review Letters **102**, 036401 (2009).

[28] C.-F. Pai, L. Liu, Y. Li, H. W. Tseng, D. C. Ralph, and R. A. Buhrman, *Spin Transfer Torque Devices Utilizing the Giant Spin Hall Effect of Tungsten*, Applied Physics Letters **101**, 122404 (2012).

[29] M. Dc et al., *Room-Temperature High Spin–Orbit Torque Due to Quantum Confinement in Sputtered BixSe(1–x) Films*, Nature Materials **17**, 800 (2018).

[30] H. Wu et al., *Room-temperature spin-orbit torque from topological surface states*, Physical Review Letters **123**, 207205 (2019).